Biophysical Journal
Article

Biophysical Society

Lysenin Toxin Membrane Insertion Is pH-Dependent but Independent of Neighboring Lysenins

Ignacio L. B. Munguira,[1] Hirohide Takahashi,[1,2] Ignacio Casuso,[1] and Simon Scheuring[1,2,*]
[1]U1006 INSERM, Université Aix-Marseille, Parc Scientifique et Technologique de Luminy, Marseille, France and [2]Departments of Anesthesiology and Physiology and Biophysics, Weill Cornell Medical College, New York, New York

ABSTRACT Pore-forming toxins form a family of proteins that act as virulence factors of pathogenic bacteria, but similar proteins are found in all kingdoms of life, including the vertebrate immune system. They are secreted as soluble monomers that oligomerize on target membranes in the so-called prepore state; after activation, they insert into the membrane and adopt the pore state. Lysenin is a pore-forming toxin from the earthworm *Eisenida foetida*, of which both the soluble and membrane-inserted structures are solved. However, the activation and membrane-insertion mechanisms have remained elusive. Here, we used high-speed atomic force microscopy to directly visualize the membrane-insertion mechanism. Changing the environmental pH from pH 7.5 to below pH 6.0 favored membrane insertion. We detected a short α-helix in the soluble structure that comprised three glutamic acids (Glu92, Glu94, and Glu97) that we hypothesized may represent a pH-sensor (as in similar toxins, e.g., Listeriolysin). Mutant lysenin still can form pores, but mutating these glutamic acids to glutamines rendered the toxin pH-insensitive. On the other hand, toxins in the pore state did not favor insertion of neighboring prepores; indeed, pore insertion breaks the hexagonal ordered domains of prepores and separates from neighboring molecules in the membrane. pH-dependent activation of toxins may represent a common feature of pore-forming toxins. High-speed atomic force microscopy with single-molecule resolution at high temporal resolution and the possibility of exchanging buffers during the experiments presents itself as a unique tool for the study of toxin-state conversion.

INTRODUCTION

Pore-forming toxins (PFTs) (1) are a family of proteins that have the ability to increase the permeability of the target membrane. These proteins are known as virulence factors of many bacteria (2,3). PFTs and, more generally, pore-forming proteins (PFPs) are, however, not only found in prokaryotes but occur in all kingdoms of life (4) and are even active in the mammalian immune system as a defense weapon (5). The action mechanism, common to all family members, starts with the secretion of a soluble monomer. The soluble form binds specifically to a target on the membrane that can be a lipid, a protein, or a sugar (1). The change in diffusion dimensionality from bulk (three-dimensional (3D)) to membrane (2D) and the membrane interactions themselves, i.e., binding to a specific, potentially clustered, target, increases the probability of a monomer-monomer encounter. The latter is conceptualized in receptor clustering in rafts (6–8). This process gives rise to the membrane-associated oligomer state, known as the prepore. In a state conversion, the toxin undergoes a large conformational change from a membrane-associated to a membrane-inserted or transmembrane protein, termed a pore. The pore is typically large and non-specific, e.g., a 3.0-nm-diameter β-barrel with a minimal constriction of 1.6 nm in the case of lysenin (9), and permeable to water, ions, large molecules, and small proteins (1,10). The transition and activation mechanisms of this conformational change have been studied for Anthrax (10) and Listeriolysin O (11,12), but they remain unclear for most PFTs.

Lysenin (13) is a PFT in the coelomic fluid of the earthworm *Eisenia foetida*. The structure of the soluble form of lysenin was solved by x-ray crystallography alone (PDB: 3ZXD) and in complex with sphingomyelin (SM) (PDB: 3ZXG) (14), and the structure of the transmembrane pore form has been solved by cryo-electron microscopy (cryo-EM) (PDB: 5GAQ) (15) and x-ray crystallography (PDB: 5EC5) (9). Lysenin was also studied by high-speed atomic force microscopy (HS-AFM) (16–18), which revealed toxin assembly, membrane domain reorganization, and glasslike diffusion in a crowded membrane. Lysenin is a soluble monomer (14) that

Submitted June 27, 2017, and accepted for publication August 11, 2017.

*Correspondence: sis2019@med.cornell.edu

Ignacio L. B. Munguira and Hirohide Takahashi contributed equally to this work.

Editor: Joseph Zasadzinski.

https://doi.org/10.1016/j.bpj.2017.08.056

binds to SM (19), a major component of lipid rafts (20). Assembly and oligomerization into a nonameric ring (18) is facilitated by cholesterol (Chol) (19). Despite the wealth of structural information about lysenin (9,14,15), little is known about the dynamic state transition and the associated activation mechanism. The conformational change that leads to pore formation is triggered by acidic pH in several PFTs (21–26). Acidic conditions that trigger the insertion are found in early endosomes (27) in the Anthrax toxin life cycle (10), or in the phagosome for listeriolysin O. Here, we set out to study the cues that drive lysenin pore formation.

AFM was successfully used to study toxins. The ability to measure under adjustable conditions and the possibility of fine-tuning the composition of the supported membrane placed AFM early on among the most useful approaches to study PFTs (28–30). Since then, AFM has repeatedly been used to study the structures of toxins in membranes (31–33). HS-AFM (34,35) provides new possibilities for the study of toxins, namely, the assessment of structure-function relationships due to the visualization of dynamics (11,16–18,36). Here, we use control of the environmental conditions during HS-AFM operation (37) to analyze the pH-dependent prepore-to-pore transition of lysenin and show how mutation of three amino acids in a putative pH sensor render the toxin pH insensitive.

MATERIALS AND METHODS

Protein purification

A complementary DNA fragment, coding for lysenin (GenBank: BAA21518.1) and its mutant (E92, 94, 97Q) were ordered from GenScript. The complementary DNA fragments were subcloned into a pET28a vector at the BamHI and Hind III sites. This vector was transformed into the BL21 (DE3) strain (New England BioLabs France, Evry, France). The transformed cells were inoculated into 1 L of LB medium containing 50 μg/mL kanamycin sulfate and incubated at 37°C with shaking at 220 rpm until the OD_{600} value reached 0.6. For induction of lysenin expression, isopropyl β-D-1-thiogalactopyranoside was added to the bacterial medium (0.5 mM final concentration) with shaking at 20°C and 200 rpm. The bacteria were collected by centrifugation at 2000 $\times$ g for 10 min. The activity of proteases was inhibited by the addition of 1 mM phenylmethane sulfonyl fluoride. To disrupt the bacteria, we performed three sonication cycles with intervals of 30 s on ice. The resultant suspension was shaken at 4°C for 30 min in the presence of 0.1% Triton X-100 and RNase/DNase at 10 μg/mL concentration. The crude extract was then centrifuged at 10,000 $\times$ g for 30 min. The supernatant (volume; typically up to 10 mL) was collected and mixed with 1 mL of chelating Nickel Ni-NTA Affinity Resin (Generon, Slough, United Kingdom) in phosphate-buffered saline (PBS) at pH 7.5. Lysenin binding to the Ni-NTA resin was performed through 1 h incubation at 4°C with gentle shaking, and the resin was washed three times with PBS containing 100 mM imidazole-HCl (pH 7.5). The lysenin was eluted with 2 mL of 250 mM imidazole-HCl. To eliminate the imidazole, the eluate was dialyzed overnight against 1 L of PBS at pH 7.5.

Sample preparation for HS-AFM observation

Egg SM and Chol (Avanti Polar Lipids, Alabaster, AL) at a molar ratio of SM/Chol 1:1 were used to form giant unilamellar vesicles (GUVs) through electroswelling (38). Of each lipid, 10 μL at 3 mM dissolved in chloroform/methanol (3:1) were deposited on a glass plate coated with indium tin oxide with ~100 Ω resistivity (Sigma-Aldrich, St. Louis, MO) and placed for 60 min in the desiccator for complete solvent evaporation. A U-shaped piece of rubber ~1 mm thick was sandwiched between two indium-tin-oxide-coated slides. The so-formed chamber was filled with ~400 μL of 200 mM sucrose solution and exposed to 1.5 V sinusoidal 10 Hz AC current for 3 h, followed by a squared 5 Hz AC current for 15 min, at 55°C. GUVs were harvested from the chamber. To form the supported lipid bilayers (SLBs) for HS-AFM, 1 μL of GUV solution was placed on a 1.5-mm-diameter freshly cleaved mica disk covered with 1 μL of PBS and incubated for 30 min. To remove lipid that was not firmly attached, the SLB was intensely rinsed with PBS. Once the bilayer was formed, 1 μL of purified lysenin was incubated for 15 min. Excess protein was again rinsed with PBS.

HS-AFM

HS-AFM movies were acquired with an HS-AFM (SS-NEX, Research Institute of Biomolecule Metrology, Tsukuba, Japan) (34) equipped with a superluminescent diode (wavelength, 750 nm; EXS 7505-B001, Exalos, Schlieren, Switzerland) and a digital high-speed lock-in Amplifier (Hinstra, Transcommers, Budapest, Hungary) (39). Cantilevers 8 μm long with nominal spring constant $k = 0.15$ N/m, resonance frequency in liquid $f_{(r)} =$ 600 kHz, and quality factor in liquid $Q_c \approx 1$ (USC-1.2, NanoWorld, Neuchâtel, Switzerland), featuring an electron beam deposition tip, were used. For high-resolution imaging, the electron beam deposition tip was sharpened by helium plasma etching using a plasma cleaner (Diener Electronic, Ebhausen, Germany), resulting in a final tip radius of ~2 nm, as judged from analysis of the indentation inside the lysenin rings. Amplitude modulation mode was used for imaging with free amplitude of ~1.2 nm and operating set-point amplitude of ~0.9 nm. Under these conditions, we calculate the applied setpoint force, F_s, according to $F_s = (k_c \bullet [(1-\alpha) \bullet (A_0^2 - A_s^2)]^{1/2}/Q_c$, where A_0 is the free amplitude, A_s is the setpoint amplitude, and $\alpha \approx 0.5$ for short cantilevers, α being the ratio ($0 < \alpha < 1$) of amplitude reduction caused by the cantilever resonance frequency shift over the total amplitude reduction (35). Under our imaging conditions, $F_s \approx 84$ pN. All experiments were performed at room temperature and in physiological buffer.

Experiment of pH change

The pH changes were achieved through addition of 3 μL of 5 mM HCl solution. The pH in the fluid cell was determined before and after HS-AFM experiments by scaling up the volumes 10-fold and measuring the pH with a pH meter (ΔpH = $\pm$0.2; HANNA instruments, Woonsocket, RI) (Movie S1), though this procedure implies uncertainties, as we ignore how well the HCl solution mixed in the HS-AFM fluid chamber. Alternatively, a pump (Harvard Instruments, Holliston, MA) was connected by two silicone tubes to the fluid cell pool cantilever holder for injecting and extracting solution (37) at a rate of 0.17 μL/s to exchange from a buffer of 20 mM HEPES (pH 7.5) and 120 mM NaCl to a buffer of 20 mM MES (pH 4.0) and 120 mM NaCl. Again the pH was determined by scaling up the experimental volumes 10-fold and measuring the pH with a pH meter (Movie S3).

HS-AFM image treatment

Image treatment of the HS-AFM movies was limited to a first-order *XY* plane fit and *XY* drift correction (40).

HS-AFM data analysis

For the pore-neighbor distribution analysis, we first determined through cross-correlation searches the center *XY*-position of each particle in

lab-developed routines in ImageJ (40,41). From these coordinates, the nearest-neighbor counts were extracted through Voronoi tessellation and Delaunay triangulation using prebuilt functions in MATLAB (The MathWorks, Natick, MA). In parallel, the same HS-AFM frames were binarized (1, 0) with a threshold height $h_{(\text{cutoff})} = (h_{(\text{average-prepore})} - h_{(\text{average-pore})})/2$ to discern prepore- from pore-state molecules. Those Vornoi cells that had a median pixel value of 1 were assigned as prepores, those with a median value of 0 were assigned as pores. Next, for each pore, the total number of neighbors and their identity as "prepore" or "pore" were counted.

RESULTS AND DISCUSSION

First, we prepared SLBs composed of SM/Chol (1:1) through vesicle fusion on the HS-AFM mica support (18), onto which we adsorbed heterologous expressed and purified wild-type (wt) lysenin. Since the amino acid sequence of the *Escherichia coli*-expressed lysenin was identical to the *E. foetida* lysenin, we reason that it has the same mechanism of action as the natural earthworm toxin. Lysenin diffused on the bilayer and formed stable hexagonal arrays on SM-enriched domains (16–18,42). These arrays could be imaged at physiological pH over extended periods without significant topographical changes. Under such conditions, only ~15% of the lysenin nonamers were in the pore state, protruding ~2.5 nm, whereas ~85% formed a hexagonal array of prepores, protruding ~5.0 nm (Fig. 1 *a*, $t = 411$ s). Decreasing the pH from 7.5 to <6.0 during the HS-AFM movie acquisition induced transition from the prepore to the pore state in many molecules, as detected in HS-AFM frames by oligomer rings that appear darker due to their ~2.5 nm decreased topography (Fig. 1 *a*; Movie S1). Statistical assessment, using a protrusion threshold of ~3.75 nm (between the prepore and pore heights), of the total areas occupied by prepores and pores, combined with cross-correlation-based particle counting revealed that the percentage of pores increased from ~15 to ~47% (Fig. 1 *b*, *black circles*). As a result of the pH change and the consecutive increase in the number of pore-state lysenins, the hexagonal array lost order and the oligomers displayed lateral dynamics. The change of topography can be assessed by the calculation of standard deviation maps (SD maps) during topography averaging (43) or as a function of time in image series (44). Calculating STD maps over five subsequent frames (Movie S2) at the times corresponding to the topography maps shown in Fig. 1, *a* and *c*, and plotting the average SD value as a function of time highlights the increase of lysenin mobility with pH drop and prepore-to-pore transition of about half of the proteins (Fig. 1 *b*, *gray triangles*). Membrane insertion was irreversible and we could not achieve pore-to-prepore transitions by elevating the pH, probably due to the outstanding stability of the β-barrel structure formed, where all backbone polar

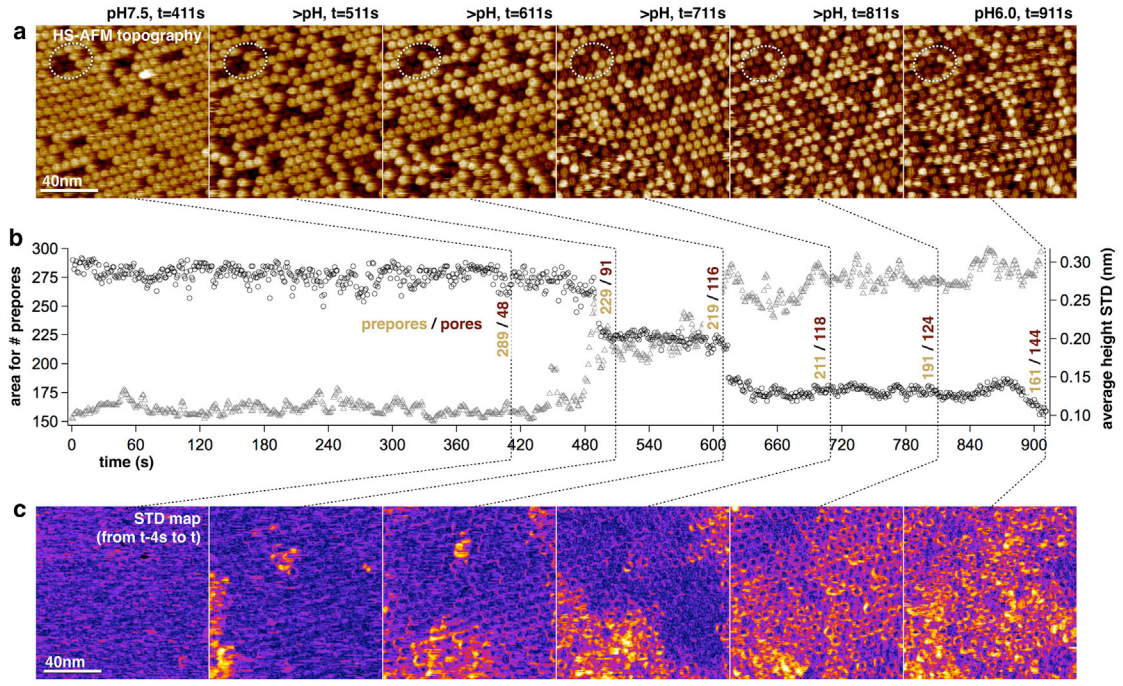

FIGURE 1 Lysenin toxin membrane insertion is pH dependent. (*a*) HS-AFM movie frames of lysenin on an SM/Chol (1:1) bilayer (Movie S1). During HS-AFM movie acquisition, the pH is changed from 7.5 to <6.0, leading to an increased number of prepore lysenins (*bright circles*, protruding 5 nm) that insert into the membrane to become pore lysenins (*dark circles*, protruding ~2.5 nm). (*b*) Graph of the number of prepores (i.e., image area occupied by pixels higher than the 3.75 nm threshold) as a function of movie acquisition time (*black circles*). The precise number of prepores and pores has been analyzed by cross-correlation searches at six specific time points (*dashed lines*) corresponding to the frames shown in (*a*). The average value of the SD maps shown in (*c*) reports about the topographical changes, i.e., the lateral mobility between subsequent frames, throughout movie acquisition. (*c*) SD maps over five consecutive frames ($t - 4$ s to t, where t is the time of recording the topography frames shown in *a*). To see this figure in color, go online.

groups are involved in β-strand-β-strand hydrogen bonds within the apolar membrane environment (45).

It has been shown by experiment, simulation, and theory that neighboring membrane proteins "feel" each other through the membrane (46). Membrane proteins are attracted toward each other in the membrane due to energy minimization of the membrane perturbations that they create in their vicinity (for a review, see (47)). We therefore hypothesized that a lysenin that underwent the prepore-to-pore transition might influence and favor the pore formation of neighboring lysenins, because the membrane environment that it created when undergoing the conformational transition is that of a pore. Such an effect would provide an additional sense to the clustering of lysenin prepores, as clustering would then result in an amplification of pore formation and hence toxicity. We therefore set out to analyze the molecular environment of each lysenin (Fig. 2).

For this, we performed cross-correlation searches to detect each oligomer in the HS-AFM images (Fig. 2 *a*). We then calculated the Voronoi tessellation of the molecular distribution (see Materials and Methods and (18)), which resulted in a field of polygons, each of which houses one lysenin oligomer and defines its number of direct neighbors (Fig. 2 *b*). Analyzing the height of the molecule within each Voronoi cell assigns its identity state as "pore" or

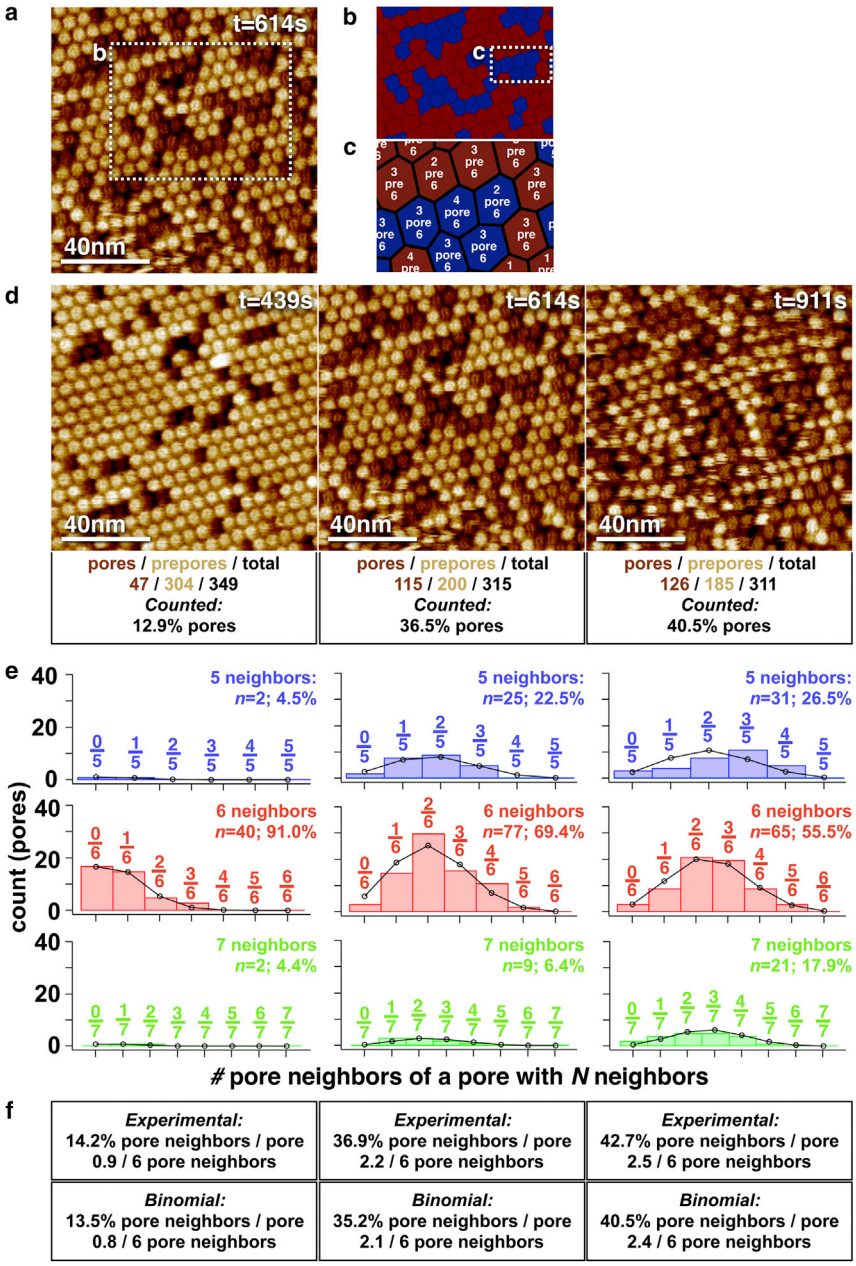

FIGURE 2 Neighbors of lysenin pores. (*a*) HS-AFM frame displaying a mixture of prepore (*bright circles*) and pore (*dark circles*) lysenins. (*b*) Voronoi tessellation of the lysenins distributed in the area outlined by a dashed rectangle in (*a*). The Voronoi cells that are occupied by pore lysenins are in blue and those occupied by prepores are in red. (*c*) Detailed view of the Voronoi tessellation in the area outlined by a dashed rectangle in (*b*). Each Voronoi cell is characterized by three parameters: 1) its identity as a pore (*blue*, "pore") or prepore (*red*, "pre"), 2) the number of pore neighbors (*top number*), and 3) the number of total neighbors (*bottom number*). (*d*) Three high-resolution HS-AFM image frames (at $t = 439$, $t = 614$, and $t = 911$ s) displaying an increasing number of pores, a decreasing number of prepores, and a decreasing total number of lysenins in the preserved image area. (*e*) Histograms of the number of pore neighbors for each pore that has five (*blue*), six (*red*), or seven (*green*) total neighbors. The three panels from left to right correspond to the three analyzed frames shown in (*d*). The black circles and lines correspond to binomial distributions with the same number of pores and prepores. (*f*) Summary of the results showing the experimental and binomial average numbers of pore neighbors of pores. To see this figure in color, go online.

"prepore" and shows the total number of neighbors it has and the number of those that are pore neighbors (Fig. 2 *c*). We analyzed in great detail representative images at three stages during the insertion process (Fig. 2 *d*). Simply counting the number of pores as a fraction of all molecules in these frames results in 12.9% (t = 439 s), 36.5% (t = 614 s), and 40.5% (t = 911 s) (Fig. 2 *d*, *bottom*). Using the above-described Voronoi tessellation procedure, we analyze for all pores that have 5 (Fig. 2 *e*, *top*), 6 (Fig. 2 *e*, *middle*), and 7 (Fig. 2 *e*, *bottom*) neighbors the number of pore neighbors they have (Fig. 2 *e*, *histograms*). We then compare these nearest-pore-neighbor distributions with expected binomial distributions of a noncooperative system for the number of neighbors and the total number of pores and molecules found in these frames (Fig. 2 *e*, *black circles*). We find a good agreement between the distributions and the average experimental values, 14.2% (t = 439 s), 36.9% (t = 614 s), and 42.7% (t = 911 s), as well as the averages from binomial distributions, 13.5% (t = 439 s), 35.2% (t = 614 s), and 40.5% (t = 911 s) (Fig. 2 *f*); all of these values also compare very well with the simple pore-counting percentages in the entire images, 12.9% (t = 439 s), 36.5% (t = 614 s), and 40.5% (t = 911 s) (see Fig. 2 *d*). In contrast, a system where lysenin pores had a significant annular cooperativity with their neighbors would result in images where one part is completely occupied by prepore lysenins and another part is completely covered by pore lysenins, and statistsics where the probability of finding pores around a pore would be much higher than the average occurrence of pores. The minor discrepancies that we found certainly emerge from the molecules located at the edges (~50), for which we ignore their neighbor identity. Thus, nearest-neighbors statistics indicated that pore insertion is, within error, noncooperative, independent of the state of the neighbor molecule. Consequent to our observations of this, and extending our understanding of the insertion behavior of lysenin, we observe that lysenin pores repel molecules in their environment. First, we found that upon membrane insertion, the molecules break out of their rigid hexagonal paracrystalline packing and their mobility increases (Fig. 1 *c*). Second, we found fewer total lysenin oligomers per membrane area upon membrane insertion, namely, 351 when most of the molecules are prepores and 311 when ~41% have transited into pores in the same image frame (Fig. 2 *d*, *left* and *right*). Third, breakage of the hexagonal array is documented by the occurrence of molecules in the membrane with five or seven neighbors, whereas in the prepore state, essentially all molecules have six neighbors (Fig. 2 *e*, *left* and *right*). Fourth, and finally, the average intermolecular distances increased from 12.5 ± 0.7 to 13.4 ± 1.2 nm (mean ± SD; $p < 0.05$) in Fig. 2 *d*, t = 439 and t = 911 s, respectively. This increase in space occupied is not due to a larger molecular diameter of the pore. First, the pore structure is of same diameter as the nonamer prepore model built from the soluble structure (Fig. 3, *a* and *b*; see also (15)). Second, at early stages of the prepore-to-pore transition, when the majority of molecules are still in the prepore state and the hexagonal packing is still stable (Fig. 1 *a*, t = 411, t = 511, and t = 611 s), pores fit well into the space between prepores. We propose, with respect to the recent cryo-EM structure that defines well the membrane-embedded region of the pore structure as a detergent-bound shell that delineates the boundaries of the lipid bilayer (15), that the pore may lose interaction between the receptor-binding domain and SM, which as a raft lipid has been shown to be relevant for clustering of the lysenin prepores; hence, pores that have lost this interaction are unordered and diffusive. We conclude that the membrane-embedded pore lysenin at slightly acidic conditions does not have a net attraction for neighboring molecules, and that this may be due to its molecular properties or be

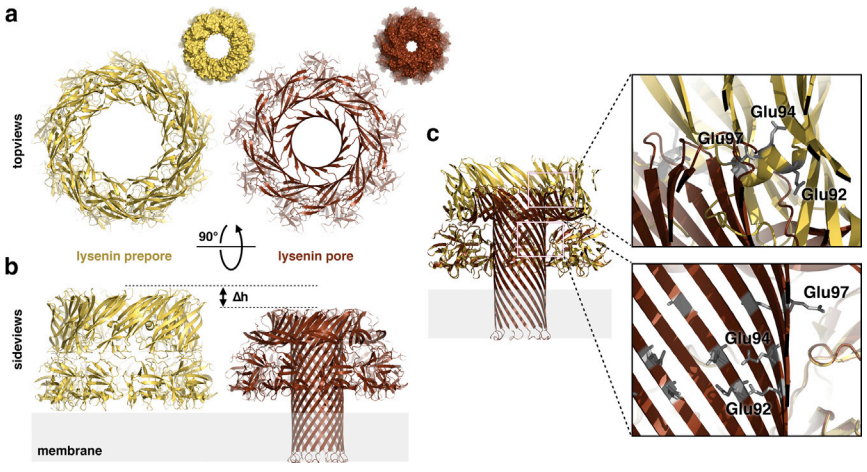

FIGURE 3 Lysenin prepore and pore structures and position of the putative pH sensor. (*a*) Top views of the lysenin prepore and pore structures and the corresponding molecular surfaces (*smaller images*). The prepore model shown here was assembled from the monomeric soluble structure (PDB: 3ZXD) aligned to the pore structure (PDB: 5GAQ) by their receptor-binding domains (residues 160–297), which are essentially identical (root mean-square deviation, 0.47 Å; 908 atoms). (*b*) Side views of (*a*). The difference in height between the models of the prepore and the pore is ~1.5 nm ((9)). In the HS-AFM topographs, the height difference is ~2.5 nm, indicating that the membrane insertion might be slightly different from what the detergent shell in the cryo-EM structure suggests (9). (*c*) View of the prepore model superimposed on the pore aligned by their structurally unchanged receptor-binding domains. Top inset: The pH sensor, the small helix comprising Glu92, Glu94, and Glu97, is exposed to the inner cylinder face of the prepore structure. Bottom inset: In the pore structure, Glu92, Glu94, and Glu97 are located about in the middle of the 97-Å-long β-barrel. To see this figure in color, go online.

an indirect consequence of its changing interactions with lipids.

From all these results, we conclude that the prepore-to-pore transition is pH driven and noncooperative—in the sense that a membrane-inserted pore does not exert positive bias on its nearest-neighbor molecules to also undergo prepore-to-pore transition—in the conditions used here, i.e., a supported SM/Chol (1:1) lipid bilayer. Furthermore, pore lysenin breaks the hexagonal clustering of the prepore lysenin on SM-enriched membrane domains due to rather repulsive environmental interactions when inserted into the membrane. Further experiments in different bilayers of different lipid composition are needed to analyze whether and to what extent other lipids will influence the lysenin prepore-to-pore transition.

To assess the molecular basis of the pH sensitivity in lysenin, we looked into the lysenin sequence and structure for a putative pH-sensor domain (Fig. 3, *a* and *b*). We found a good candidate in three glutamic acid residues, Glu92, Glu94, and Glu97, that are located in a short (the only) α-helix in the lysenin prepore structure (Fig. 3 *c*, *top inset*; see also (14)). It is noteworthy that the prepore-to-pore transition implies a full conversion of α-helical elements to β-strands; there are no α-helical secondary-structure elements remaining in the pore structure (9,15). The characteristics of the putative lysenin pH sensor are very similar to the pH sensor in Listeriolysin (48,49). To test the influence of this glutamic-acid triad on pH sensing, we mutated the three glutamic acids to glutamines, i.e., E92Q, E94Q, and E97Q; we refer to this mutant as EQ-lysenin in the reminder of the text. The underlying idea is that the glutamic acids are negatively charged at physiological pH and become neutral while being protonized. Suggesting that this switch might favor the prepore-to-pore conformational change, substitution of the glutamic acids by glutamines would cause these amino acids to be not protonizable and, as a consequence, would render the protein pH-insensitive.

To test the pH sensitivity of EQ-lysenin, we performed the HS-AFM experiments as described above for the wt-lysenin (Fig. 4). Starting at pH 7.5, we imaged EQ-lysenin on SM/Chol (1:1) bilayers. At the resolution of HS-AFM, we could not detect any structural differences between the wt- and EQ-lysenin. After the pH drop to reach pH 4.3, the HS-AFM movie frames did not reveal an increased number of pores (Fig. 4 *a*). Cross-correlation-based particle counting revealed a constant number of ~500 prepores and ~150 pores throughout the experiment (Fig. 4 *b*). We concluded that the short α-helix with sequence TETEVYE, and notably the three glutamic acids in it, contributes to the lysenin conformational transition and pH sensitivity, respectively. Probably, protonation of Glu92, Glu94, and Glu97 facilitates the transition of the α-helix to a β-strand and hence favors formation of the transmembrane β-barrel.

CONCLUSIONS

The ability of HS-AFM to distinguish prepore and pore lysenin under adjustable physiological conditions allowed us to study lysenin pH sensitivity with respect to its prepore-to-pore transition at the single-molecule level. HS-AFM has the additional ability to image nonlabeled proteins, meaning that not only the particle of interest but also its environment is captured.

We show that a decrease from pH 7.5 to below pH 6.0 is sufficient to favor lysenin membrane insertion, probably due to protonation of a pH-sensor domain, i.e., the three glutamic acids Glu92, Glu94, and Glu97. A similar pH sensor

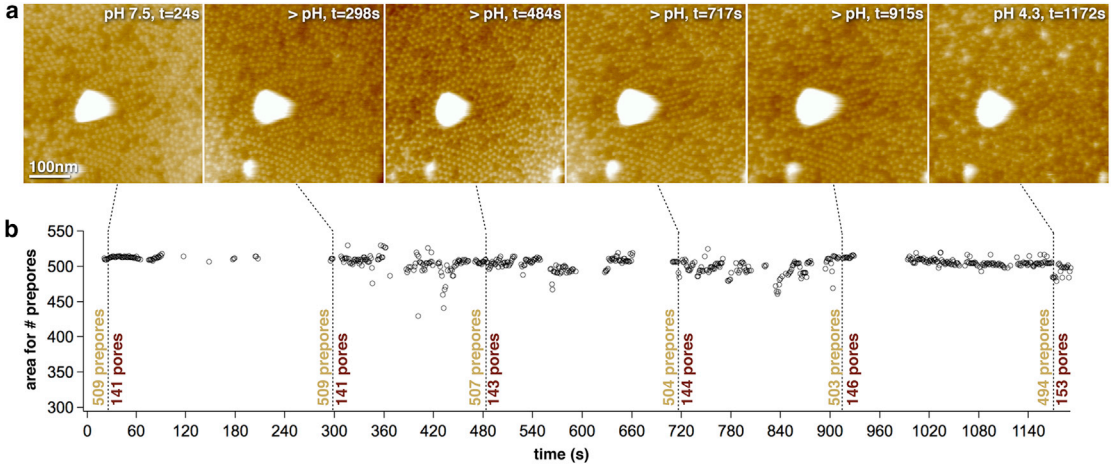

FIGURE 4 EQ-lysenin is pH insensitive. (*a*) HS-AFM movie frames of EQ-lysenin on an SM/Chol (1:1) bilayer (Movie S3). During HS-AFM movie acquisition, the pH was changed from 7.5 to 4.3, without a significant effect on the membrane insertion of the EQ-lysenin prepores. (*b*) Graph of the number of prepores (i.e., image area occupied by pixels higher than the 3.75 nm threshold) as a function of movie acquisition time. The precise number of prepores and pores has been analyzed by cross-correlation searches at six specific time points (*dashed lines*) corresponding to the frames shown in (*a*). To see this figure in color, go online.

has been reported in listeriolysin O (48,49). Given the structural similarities of lysenin to the aerolysin family (14), we hypothesize that a similar activation mechanism may exist for the entire family. These observations are, to our knowledge, the first direct evidence of pore formation of a toxin from the aerolysin family. Facilitated membrane insertion as a result of a pH decrease has been described for many toxins, such as anthrax toxin from *Bacillus anthracis*, listeriolysin from *Listeria monocytogenes*, perfringolysin from *Clostridium perfringens*, VacA from *Helicobacter pylori*, and diphtheria toxin from *Corynebacterium diphtheriae* (10,21–26). Hence, we could well look at a conserved activation mechanism of PFTs. It is, however, notable that, in contrast to the above-cited prokaryotic toxins, lysenin emerges from the coelomic fluid of the earthworm *E. foetida.* Indeed, the in vivo function of lysenin remains enigmatic: It has been proposed that lysenin would protect the earthworm from bacterial infections, though this concept is challenged by the fact that bacteria are devoid of SM. However, lysenin showed antibacterial action, albeit the cytolytic activity was much slower than on erythrocytes or SM-containing membranes, indicating some nonspecificity concerning the membrane target (50). Another hypothesis would be that higher animals with SM-containing cell membranes would seriously suffer from ingesting earthworms, especially, as we show here, when the toxin is activated at a low pH, such as in gastric environments, and hence would be discouraged from further ingestion of earthworms.

We also found that membrane insertion was noncooperative, as we did not detect a positive bias for molecules that were nearest neighbors to a pore to undergo prepore-to-pore transition themselves. Furthermore, lysenin membrane insertion significantly changes the properties of lysenin with its environment, specifically changing it from clustering of the prepores to a rather repulsive regime for the pores. However, we cannot exclude the possibility that the pH change itself led to a repulsion between the molecules in general. We propose the following putative mechanism underlying this observation. It is known that the prepore structure binds with its receptor-binding domain to SM, which is a raft-type lipid and has been shown to be relevant for clustering of the lysenin prepores (17). After pore formation, the receptor-binding domain is elevated from the membrane, as reported by the position of the detergent shell in the cryo-EM structure (15), probably breaking the interaction of the lysenin receptor-binding domain with the membrane-embedded SM. As a result of the loss of interaction with the raft-lipid SM, lysenin might lose its tendency to cluster (17). This loss of interaction with the raft-lipid SM may also be the basis of the increased diffusion of the pores that can be seen at the end of Movie S1. Alternatively, one could suggest that the hydrophobic thickness of the transmembrane region of pore lysenin of ~27 Å was in good agreement with the hydrophobic thickness of the SM/Chol bilayer, hence not creating a net attraction between molecules due to membrane-deformation-related energy minimization.

In conclusion, we show that the lysenin prepore-to-pore transition is pH dependent and neighbor noncooperative, and we highlight the power of HS-AFM to study directly the structural transition of toxins in action.

SUPPORTING MATERIAL

Three movies are available at http://www.biophysj.org/biophysj/supplemental/S0006-3495(17)31015-9.

AUTHOR CONTRIBUTIONS

S.S., I.L.B.M., and H.T. conceived the experiments. I.L.B.M. and I.C. performed HS-AFM experiments. I.L.B.M., I.C., and S.S. analyzed the HS-AFM data. H.T. prepared DNA constructs, purified, and characterized the wt-lysenin and the EQ-lysenin. I.L.B.M. and S.S. wrote the article.

ACKNOWLEDGMENTS

The authors thank Professors Gregor Anderluh and James N. Sturgis for fruitful discussions. This work was funded by the Agence Nationale de la Recherche grant A*MIDEX (ANR-11-IDEX-0001-02) and a European Research Council (ERC) grant (#310080; MEM-STRUCT-AFM).

REFERENCES

1. Dal Peraro, M., and F. G. van der Goot. 2016. Pore-forming toxins: ancient, but never really out of fashion. *Nat. Rev. Microbiol.* 14:77–92.
2. Abrami, L., B. Kunz, and F. G. van der Goot. 2010. Anthrax toxin triggers the activation of *src*-like kinases to mediate its own uptake. *Proc. Natl. Acad. Sci. USA.* 107:1420–1424.
3. Bavdek, A., R. Kostanjšek, …, G. Anderluh. 2012. pH dependence of listeriolysin O aggregation and pore-forming ability. *FEBS J.* 279:126–141.
4. Szczesny, P., I. Iacovache, …, M. Grynberg. 2011. Extending the aerolysin family: from bacteria to vertebrates. *PLoS One.* 6:e20349.
5. Podack, E. R., J. D. Young, and Z. A. Cohn. 1985. Isolation and biochemical and functional characterization of perforin 1 from cytolytic T-cell granules. *Proc. Natl. Acad. Sci. USA.* 82:8629–8633.
6. Simons, K., and M. J. Gerl. 2010. Revitalizing membrane rafts: new tools and insights. *Nat. Rev. Mol. Cell Biol.* 11:688–699.
7. Jacobson, K., O. G. Mouritsen, and R. G. W. Anderson. 2007. Lipid rafts: at a crossroad between cell biology and physics. *Nat. Cell Biol.* 9:7–14.
8. Rivas, G., and A. P. Minton. 2016. Macromolecular crowding in vitro, in vivo, and in between. *Trends Biochem. Sci.* 41:970–981.
9. Podobnik, M., P. Savory, …, G. Anderluh. 2016. Crystal structure of an invertebrate cytolysin pore reveals unique properties and mechanism of assembly. *Nat. Commun.* 7:11598.
10. Young, J. A., and R. J. Collier. 2007. Anthrax toxin: receptor binding, internalization, pore formation, and translocation. *Annu. Rev. Biochem.* 76:243–265.
11. Ruan, Y., S. Rezelj, …, S. Scheuring. 2016. Listeriolysin O membrane damaging activity involves arc formation and lineaction—implication for listeria monocytogenes escape from phagocytic vacuole. *PLoS Pathog.* 12:e1005597.

12. Schnupf, P., and D. A. Portnoy. 2007. Listeriolysin O: a phagosome-specific lysin. *Microbes Infect.* 9:1176–1187.
13. Sekizawa, Y., K. Hagiwara, …, H. Kobayashi. 1996. A novel protein, lysenin, that causes contraction of the isolated rat aorta: its purification from the coleomic fluid of the earthworm, *Eisenia foetida*. *Biomed. Res.* 17:197–203.
14. De Colibus, L., A. F. Sonnen, …, R. J. Gilbert. 2012. Structures of lysenin reveal a shared evolutionary origin for pore-forming proteins and its mode of sphingomyelin recognition. *Structure.* 20:1498–1507.
15. Bokori-Brown, M., T. G. Martin, …, C. G. Savva. 2016. Cryo-EM structure of lysenin pore elucidates membrane insertion by an aerolysin family protein. *Nat. Commun.* 7:11293.
16. Yilmaz, N., T. Yamada, …, T. Kobayashi. 2013. Real-time visualization of assembling of a sphingomyelin-specific toxin on planar lipid membranes. *Biophys. J.* 105:1397–1405.
17. Yilmaz, N., and T. Kobayashi. 2015. Visualization of lipid membrane reorganization induced by a pore-forming toxin using high-speed atomic force microscopy. *ACS Nano.* 9:7960–7967.
18. Munguira, I., I. Casuso, …, S. Scheuring. 2016. Glasslike membrane protein diffusion in a crowded membrane. *ACS Nano.* 10:2584–2590.
19. Ishitsuka, R., and T. Kobayashi. 2007. Cholesterol and lipid/protein ratio control the oligomerization of a sphingomyelin-specific toxin, lysenin. *Biochemistry.* 46:1495–1502.
20. Pike, L. J. 2003. Lipid rafts: bringing order to chaos. *J. Lipid Res.* 44:655–667.
21. Jiang, J., B. L. Pentelute, …, Z. H. Zhou. 2015. Atomic structure of anthrax protective antigen pore elucidates toxin translocation. *Nature.* 521:545–549.
22. Schuerch, D. W., E. M. Wilson-Kubalek, and R. K. Tweten. 2005. Molecular basis of listeriolysin O pH dependence. *Proc. Natl. Acad. Sci. USA.* 102:12537–12542.
23. Nelson, L. D., A. E. Johnson, and E. London. 2008. How interaction of perfringolysin O with membranes is controlled by sterol structure, lipid structure, and physiological low pH: insights into the origin of perfringolysin O-lipid raft interaction. *J. Biol. Chem.* 283:4632–4642.
24. Czajkowsky, D. M., H. Iwamoto, …, Z. Shao. 1999. The vacuolating toxin from *Helicobacter pylori* forms hexameric pores in lipid bilayers at low pH. *Proc. Natl. Acad. Sci. USA.* 96:2001–2006.
25. Sandvig, K., and S. Olsnes. 1980. Diphtheria toxin entry into cells is facilitated by low pH. *J. Cell Biol.* 87:828–832.
26. Meusch, D., C. Gatsogiannis, …, S. Raunser. 2014. Mechanism of Tc toxin action revealed in molecular detail. *Nature.* 508:61–65.
27. Mellman, I. 1996. Endocytosis and molecular sorting. *Annu. Rev. Cell Dev. Biol.* 12:575–625.
28. Mou, J., J. Yang, and Z. Shao. 1995. Atomic force microscopy of cholera toxin B-oligomers bound to bilayers of biologically relevant lipids. *J. Mol. Biol.* 248:507–512.
29. Yang, J., J. Mou, and Z. Shao. 1994. Structure and stability of pertussis toxin studied by in situ atomic force microscopy. *FEBS Lett.* 338:89–92.
30. Yang, J., L. K. Tamm, …, Z. Shao. 1993. New approach for atomic force microscopy of membrane proteins. The imaging of cholera toxin. *J. Mol. Biol.* 229:286–290.
31. Mulvihill, E., K. van Pee, …, Ö. Yildiz. 2015. Directly observing the lipid-dependent self-assembly and pore-forming mechanism of the cytolytic toxin listeriolysin O. *Nano Lett.* 15:6965–6973.
32. Leung, C., N. V. Dudkina, …, B. W. Hoogenboom. 2014. Stepwise visualization of membrane pore formation by suilysin, a bacterial cholesterol-dependent cytolysin. *eLife.* 3:e04247.
33. Czajkowsky, D. M., J. Sun, and Z. Shao. 2015. Single molecule compression reveals intra-protein forces drive cytotoxin pore formation. *eLife.* 4:e08421.
34. Ando, T., N. Kodera, …, A. Toda. 2001. A high-speed atomic force microscope for studying biological macromolecules. *Proc. Natl. Acad. Sci. USA.* 98:12468–12472.
35. Ando, T., T. Uchihashi, and S. Scheuring. 2014. Filming biomolecular processes by high-speed atomic force microscopy. *Chem. Rev.* 114:3120–3188.
36. Yilmaz, N., and T. Kobayashi. 2016. Assemblies of pore-forming toxins visualized by atomic force microscopy. *Biochim. Biophys. Acta.* 1858:500–511.
37. Miyagi, A., C. Chipot, …, S. Scheuring. 2016. High-speed atomic force microscopy shows that annexin V stabilizes membranes on the second timescale. *Nat. Nanotechnol.* 11:783–790.
38. Angelova, M. I., and D. S. Dimitrov. 1986. Liposome electroformation. *Faraday Discuss. Chem. Soc.* 81:303–311.
39. Colom, A., I. Casuso, …, S. Scheuring. 2013. A hybrid high-speed atomic force-optical microscope for visualizing single membrane proteins on eukaryotic cells. *Nat. Commun.* 4:2155.
40. Husain, M., T. Boudier, …, S. Scheuring. 2012. Software for drift compensation, particle tracking and particle analysis of high-speed atomic force microscopy image series. *J. Mol. Recognit.* 25:292–298.
41. Fechner, P., T. Boudier, …, S. Scheuring. 2009. Structural information, resolution, and noise in high-resolution atomic force microscopy topographs. *Biophys. J.* 96:3822–3831.
42. Kulma, M., M. Hereć, …, A. Sobota. 2010. Sphingomyelin-rich domains are sites of lysenin oligomerization: implications for raft studies. *Biochim. Biophys. Acta.* 1798:471–481.
43. Müller, D. J., D. Fotiadis, and A. Engel. 1998. Mapping flexible protein domains at subnanometer resolution with the atomic force microscope. *FEBS Lett.* 430:105–111.
44. Rangl, M., A. Miyagi, …, S. Scheuring. 2016. Real-time visualization of conformational changes within single MloK1 cyclic nucleotide-modulated channels. *Nat. Commun.* 7:12789.
45. Wimley, W. C. 2003. The versatile β-barrel membrane protein. *Curr. Opin. Struct. Biol.* 13:404–411.
46. Casuso, I., P. Sens, …, S. Scheuring. 2010. Experimental evidence for membrane-mediated protein-protein interaction. *Biophys. J.* 99:L47–L49.
47. Phillips, R., T. Ursell, …, P. Sens. 2009. Emerging roles for lipids in shaping membrane-protein function. *Nature.* 459:379–385.
48. Köster, S., K. van Pee, …, Ö. Yildiz. 2014. Crystal structure of listeriolysin O reveals molecular details of oligomerization and pore formation. *Nat. Commun.* 5:3690.
49. Kisovec, M., S. Rezelj, …, G. Anderluh. 2016. Engineering a pH responsive pore forming protein. *Sci. Rep.* 7:42231.
50. Bruhn, H., J. Winkelmann, …, M. Leippe. 2006. Dissection of the mechanisms of cytolytic and antibacterial activity of lysenin, a defence protein of the annelid *Eisenia fetida*. *Dev. Comp. Immunol.* 30:597–606.